Title

Reversible writing of high-mobility and high-carrier-density doping patterns in two-dimensional van der Waals heterostructures

Journal

Nature Electronics, 3(2)

ISSN

2520-1131

Authors

Shi, W

Kahn, S

Jiang, L

et al.

Publication Date

2020-02-01

DOI

10.1038/s41928-019-0351-x

Peer reviewed

Reversible writing of high mobility and high carrier density doping patterns in two-dimensional van der Waals heterostructures

Wu Shi[1,2,3], Salman Kahn[1,2,3], Lili Jiang[1,2,3], Sheng-Yu Wang[1,2,3], Hsin-Zon Tsai[1,2,3], Dillon Wong[1,2,3], Takashi Taniguchi[4], Kenji Watanabe[4], Feng Wang[1,2,3], Michael Crommie[1,2,3], Alex Zettl[1,2,3,*]

[1]*Department of Physics, University of California, Berkeley, California 94720, USA*

[2]*Materials Sciences Division, Lawrence Berkeley National Laboratory, Berkeley, California 94720, USA*

[3]*Kavli Energy NanoSciences Institute at the University of California and the Lawrence Berkeley National Laboratory, Berkeley, California 94720, USA*

[4]*National Institute for Materials Science, 1-1 Namiki, Tsukuba 305-0044, Japan*

*Correspondence to: azettl@berkeley.edu

A key feature of two-dimensional materials is that the sign and concentration of their carriers can be externally controlled with techniques such as electrostatic gating. However, conventional electrostatic gating has limitations, including a maximum carrier density set by the dielectric breakdown, and ionic liquid gating and direct chemical doping also suffer from drawbacks. Here, we show that an electron-beam doping technique can be used to reversibly write high-resolution doping patterns in hexagonal boron nitride encapsulated graphene and molybdenum disulfide (MoS_2) van der Waals heterostructures. The MoS_2 device exhibits an order of magnitude decrease of subthreshold swing after doping,

whereas the doped graphene devices demonstrate a previously inaccessible regime of high carrier concentration and high mobility, even at room temperature. We also show that the approach can be used to write high-quality p-n junctions and nanoscale doping patterns, illustrating that the technique can create nanoscale circuitry in van der Waals heterostructures.

Externally controlled modulation of charge density is at the heart of the semiconductor electronics industry[1]. Modulation via traditional electrostatic gating has been shown to be effective for two-dimensional (2D) materials[2,3], but fundamental challenges remain in achieving ultra-high carrier concentration beyond the dielectric breakdown limit and in precisely defining local charge modulation with a nanoscale spatial resolution[4–8]. Although alternative doping methods such as electrolyte gating and chemical intercalation[9–12] are capable of inducing high carrier densities, they inevitably introduce disorder and unintentional electrochemical reactions which degrade device mobility[13,14]. Additionally, these methods are not suitable for local charge modulation and realistic commercial device implementation. Other techniques, such as using lithographically defined gates[4–8] or molecular self-assemblies on surfaces[15,16], can achieve impressive spatially controlled charge doping, but they cannot achieve simultaneous high carrier concentrations. They face additional limitations in applications that require rewritability or complex circuit designs.

Recent developments in van der Waals (vdW) heterostructures have led to alternate approaches to doping/gating that do not require complex processing masks or resists, with possible high mobility and high carrier concentration. For example, photo-induced

47 doping and doping using voltage pulses from the tip of a scanning tunneling microscope
48 (STM) have been demonstrated[17,18]. Both methods operate by activating defects within a
49 hexagonal boron nitride (BN) layer[19] that electrostatically influences the adjacent
50 graphene layer. While intriguing, these methods suffer from limited spatial resolution or
51 cannot be scaled to the mesoscopic lengths. Some attempts have also been made to
52 achieve n- and p-doping in graphene and other two-dimensional materials via more
53 flexible electron-beam (e-beam) irradiation using a scanning electron microscope
54 (SEM)[20–24]. The focused e-beam also enables direct writing of doping patterns into a
55 single graphene layer[20,22,23]. However, these efforts have faced common challenges
56 including unstable doped states, inevitable degradation of device quality, and limited
57 controllability of doping concentrations[20–24].

58 In this Article, we report a fully reversible e-beam doping scheme for graphene and
59 MoS_2 vdW heterostructures. We employ a BN encapsulated device geometry, which
60 protects the 2D materials from direct e-beam irradiation[25] and enables non-volatile
61 doping that is further controlled by a back-gate electric field. With this approach, we can
62 precisely tune the carrier density in the 2D materials in pre-selected spatially defined
63 regions with nanoscale resolution. The doping regions persist even after the e-beam and
64 back-gate voltage are removed, and are entirely rewritable. Importantly, we achieve high
65 electron and hole carrier densities beyond $\pm 10^{13}$ cm^{-2} in a single back-gate
66 BN/graphene/BN heterostructure device while maintaining ultra-high room-temperature
67 mobility at the theoretical phonon-scattering limit[26]. We also realize similar doping
68 effects in MoS_2 device with decreased subthreshold swing (SS) compared with the device
69 before doping.

Electron beam doping scheme and electrical measurements

The experimental scheme for the combined e-beam/back-gate doping technique is illustrated in Fig. 1 (see Methods). Doping is performed in a standard SEM with electrical feedthroughs, which allow for *in-situ* transport measurements. All graphene and MoS_2 devices are encapsulated by BN layers. This avoids depositing contaminants or e-beam induced reactions on the graphene or MoS_2 surface which can introduce disorder and degrade mobility[25]. The heterostructure is in vacuum at room temperature and the SEM-generated e-beam, with energy ranging from 1 keV to 30 keV, is used for exposure.

Figs. 1b, c illustrates the e-beam induced doping effect in graphene. The graphene device is initially largely undoped and its charge neutral point (CNP) V_{CNP} is close to 0 V. With applied V_G = 30 V the device resistance R drops from 1.2 kΩ at the CNP to 180 Ω as the back-gate field moves the device off of the CNP. At time t = 10 s (Fig. 1b), the 1 keV SEM e-beam is turned on and scanned over the entire device (see Methods) while V_G is maintained at the preset voltage V_{SET} = 30 V. As Fig. 1b shows, within several seconds R increases (also see Supplementary Note 5 and Fig. S6) and saturates near ~1.4 kΩ, close to the pre-doped CNP resistance of 1.2 kΩ. At t = 40 s the e-beam is blanked, but R remains locked and high at 1.4 kΩ; the device is now stably doped. As shown in Fig. 1c, the CNP has been shifted by 30V after exposure, equal to V_{SET} applied during the doping process. The same doping process is also applicable to MoS_2 transistor devices, as shown in Fig. 1d, e, f. The monolayer (ML) MoS_2 device is initially electron doped with a threshold voltage V_{TH} = -33 V. After a 1 keV e-beam exposure at V_{SET} = 0 V (Fig. 1e), the V_{TH} is shifted to 0 V (Fig.1f). The graphene retains a very high field-effect mobility of

~ 5 x 10^4 $cm^2V^{-1}s^{-1}$, and the MoS_2 also retains a high mobility of ~ 130 $cm^2V^{-1}s^{-1}$ at room temperature. Notably, the graphene response curve after doping is even slightly sharper than the initial curve (Fig.1c) and the subthreshold swing of the MoS_2 device is one order of magnitude smaller after e-beam doping (see Supplementary Note 3 and Fig. S3 - S4), indicating an overall reduction of charge inhomogeneity in the devices.

Gate bias and energy dependence of electron-beam induced doping

By employing different V_{SET} values during the doping process, pre-selected doping levels can be "written" into the device. The process can be applied multiple times (with different V_{SET}) to the same device and is fully reversible. Fig. 2a and 2b show respectively the transport characteristics of the same graphene and MoS_2 devices after successive doping with a 1 keV e-beam with different V_{SET}, respectively. The 1 keV e-beam induced doping causes a shift of the CNP (ΔV_{CNP}) or threshold voltage (ΔV_{TH}) close to the V_{SET} value both for electron and hole doping with the polarity controlled by V_{SET}. Remarkably, all transfer curves preserve the same sharp features, indicating little device degradation even after multiple exposures with a 1 keV e-beam. This is in clear contrast to previous e-beam doping reports that all showed inevitable mobility degradation[20–24]. Notably, our e-beam doping does not cause a 2*H* to 1*T* phase transition[27,28] in MoS_2 (see Supplementary Note 18 and Fig. S27) due to the low dosage exposure and BN encapsulation, in contrast to previous reports[20].

The e-beam doping process is sensitive to the e-beam energy. Even for the same device, doping achieved using an e-beam energy of 30 keV is qualitatively different than that obtained using an e-beam energy of 1 keV, suggesting different mechanisms behind

doping with a 1 keV beam versus a 30 keV beam. Figs. 2c and 2d show the transport properties of the same graphene and MoS_2 devices after 30 keV e-beam induced doping with different V_{SET}. Hysteresis and leakage current measurements are presented in SI (Supplementary Note 6 and Figs. S13 - S14). Here, for a given V_{SET}, we observe an opposite doping effect in Fig. 2c compared to the 1 keV case in Fig. 2a. When a positive V_{SET} is applied, the graphene CNP shifts to a negative value, corresponding to *n*-doping (whereas a positive V_{SET} leads to *p*-doping in the 1 keV case). Moreover, the CNP is shifted to a much larger value than $|V_{SET}|$, indicating a higher doping concentration induced using a 30 keV e-beam doping than for the 1 keV case. For 30 keV e-beam doping, the field-effect mobility shows a slight doping dependence, but the sample still achieves a remarkably high room-temperature mobility, with $\mu_{FET} \approx 3 \times 10^4$ $cm^2V^{-1}s^{-1}$ for a doping concentration of $\pm 5 \times 10^{12}$ cm^{-2} (Supplementary Note 2 and Fig. S2). 30 keV e-beam doping can induce highly doped states even beyond $\pm 1 \times 10^{13}$ cm^{-2} with relatively small V_{SET} values. For example, as shown in Fig. 2c, the graphene device can be highly doped and the CNP moved far beyond -80 V for V_{SET} = 30 V. Fig. 2d shows a similar doping effect in MoS_2 for the 30 keV e-beam exposure. A highly electron-doped state is achieved for V_{SET} = 30 V (red curve in Fig. 2d), the opposite of what occurs in the 1 keV case (Fig. 2b). We also observed a reduction of the field-effect mobility for V_{SET} = -45 V, which further indicates that high-energy e-beam exposure causes doping in devices through a different mechanism than low-energy e-beam exposure. We note that the e-beam induced doping effects are reproducible and repeatable in multiple devices and for multiple cycles (Supplementary Note 1, Note 7, Fig. S1 and Fig. S15). Moreover, the

doped device is quite stable even in an ambient environment (Supplementary Note 5 and Figs. S7 - S12).

Electrical characterization of highly doped devices

Next, we focus on the BN/Gr/BN heterostructure and characterize the device performance after e-beam induced doping. We employ Hall effect measurements to determine explicitly the doping concentrations and mobilities for both highly *n*- and *p*-doped states (Supplementary Note 4 and Fig. S5). For 30 keV e-beam doping, the doping concentration easily reaches ~1.7 x 10^{13} cm^{-2} for *n*-doping and ~ -1 x 10^{13} cm^{-2} for *p*-doping. Such high carrier concentrations cannot typically be achieved with conventional SiO_2 back-gated devices, as the required back-gate voltage would greatly exceed the breakdown voltage of the BN/SiO_2 dielectric. Fig. 3a shows the Hall mobility μ_{Hall} as a function of carrier density n_{Hall} for both *n*- and *p*-doped devices induced by 30 keV e-beam doping. The Hall mobility at 300 K is close to 10^4 $cm^2V^{-1}s^{-1}$ for a doping concentration of 1.7 x 10^{13} cm^{-2}, comparable to the acoustic-phonon-limited mobility predicted for intrinsic graphene[26,29,30] (Supplementary Note 10). The room-temperature mobility reported here in the high carrier density regime beyond ±5 x 10^{12} cm^{-2} (outside the shaded region in Fig. 3a) is much higher than in other reports, even five times higher than the mobility accessed by ionic liquid gating[10], electrolyte gating[9] and lithium intercalation[12] on monolayer graphene devices (Fig. 3a).

In the high carrier density regime, the four-terminal sheet resistivity ρ for our devices is ~40 ohms per square (Fig. 3b) at 300 K, comparable to the record sheet resistivity for graphene[9,30]. As shown in Fig. 3b, ρ decreases monotonically with

temperature for both electron and hole-doped devices, showing metallic behavior. It follows a linear T dependence in the high-temperature regime (30 K < T < 160 K) and saturates to a very low residual resistance in the low-temperature limit[9,12,30]. This reflects the cleanness of our device even in the high-density regime. Fig. 3c shows well-defined Shubinikov-de Haas (SdH) oscillations in the same electron-doped device at temperature 2 K with a carrier density n_{SdH} of 1.28 x 10^{13} cm^{-2}, consistent with n_{Hall}. The Hall effect mobility at 2 K reaches 10^5 $cm^2V^{-1}s^{-1}$. This reflects a homogeneous, high density, ultra-high mobility two-dimensional electron gas (2DEG) in our device.

Direct electron-beam writing of nanoscale doping patterns

The e-beam activation process enables the writing of spatially complex doping patterns with high resolution in a single vdW heterostructure device, without the need for complex gating electrodes, ionic fluids, or deposition of foreign chemical species. By using the lithography function in the SEM, the electron beam can be positioned to different target regions and thereby be used to draw arbitrary patterns with nanoscale precision. Here we demonstrate the creation of a high-quality graphene p-n junction by e-beam induced doping. As shown in the inset of Fig. 3d, we use the lithography mode of the SEM to selectively expose the region enclosed by the red rectangle and the blue rectangle to a 2 keV e-beam while holding V_{SET} to ~ -20 V and 20 V, respectively. These two regions thus respectively become electron and hole doped. Two distinct sharp peaks are observed when measuring electrical resistance across the whole device, showing a separation of the CNP of ~ 40 V. This is the clear characteristic feature of a high-quality graphene p-n junction, vastly superior to those obtained in previous reports[15,17,23]. The p-n

junction is further investigated at low temperature. While in the quantum Hall regime, there are three distinct regions that can be tuned into with the global back-gate: p-p, p-n and n-n. Fig. 3e shows the longitudinal resistance across the p-n junction while varying the magnetic field and the carrier density. In the p-n junction region, the longitudinal resistance jumps into an insulating state due to the quantum Hall edge states counterpropagating and interfering with each other[4,15]. While in the p-p region and n-n region, there are edge states that propagate in the same direction and mix in the channel as manifested in the Landau fan diagram. This proves our technique preserves the high mobility of the device after patterning and can be used to engineer quantum states. Moreover, it is highly reconfigurable and a p-i-n junction is also created after erasing the previously written p-n junction in the same device (Supplementary Note 7 and Fig. S16).

The lithography mode of the SEM allows the writing of more sophisticated doping patterns at high spatial resolution down to 200 nm. We use scattering-type scanning near-field optical microscopy (s-SNOM) and electrostatic force microscopy (EFM) to image some of the patterns we have created (see Methods). Figs. 3f and 3g show s-SNOM images of a stripe pattern and a letter "B" pattern drawn using the e-beam lithography mode with V_{SET} = 55 V and a beam energy of 2 keV (see dosage parameters in SI). The s-SNOM image clearly reveals a striped doping modulation (Supplementary Note 8 and Fig. S17) resulting from different scattering amplitudes of the infrared light in response to different local carrier densities. The letter "B" pattern has a line width of ~ 200 nm, a significant improvement over previous results[17,19]. This spatial resolution is confirmed with our EFM measurement (Supplementary Note 9 and Fig. S18). We remark that our

206 intrinsic doping line width may be even smaller, since our EFM analysis neglects line
207 charge electric field divergence.
208
209 ## Proposed doping mechanism
210 We now turn to the e-beam energy-dependent doping mechanism. It is revealing to
211 plot the normalized effective capacitance $\Delta V_{CNP}/V_{SET}$ and $\Delta V_{TH}/V_{SET}$ vs V_{SET}
212 (proportional to the electric field) for the graphene and MoS_2 devices as shown in Fig. 4a
213 and 4b, respectively. For low beam energy (1 keV) exposures, $\Delta V_{CNP}/V_{SET}$ and $\Delta V_{TH}/V_{SET}$
214 remain nearly constant at unity, independent of V_{SET}. For higher beam energy (>> 1 keV)
215 exposures, $\Delta V_{CNP}/V_{SET}$ and $\Delta V_{TH}/V_{SET}$ are strongly dependent on V_{SET} and the e-beam
216 energy. Doping with a 30 keV exposure results in an effective capacitance is more than
217 four times higher than the dielectric capacitance for electron doping. This indicates an
218 electric-field and irradiation boosted charge accumulation process. MoS_2 exhibits an
219 asymmetric behavior and here it is more difficult to access hole conduction compared to
220 graphene, possibly because MoS_2 has a large band gap and the device is intrinsically
221 electron doped. Nevertheless, the similar energy and electric field dependence of the
222 doping effects suggests a general doping mechanism for our e-beam doping process in
223 vdW heterostructures.
224 Here we propose a preliminary model for the doping mechanism but a full
225 quantitative understanding requires further experimental and theoretical study. During e-
226 beam exposure of the vdW heterostructures, there are a variety of processes occurring
227 (secondary electron emission, plasmon decay, etc.)[31] but the primary effects that
228 contribute to the doping are electron-hole pair generation and trap states in the

dielectrics[32]. Taking graphene as an example, for low e-beam energy (1 keV and 2 keV), the electron beam primarily excites electron-hole pairs in bottom BN layers (see Supplementary Note 12 and Fig. S20), i.e., the e-beam penetration depth, d_p, is smaller than the BN thickness d_{BN} (Fig. 4c). For the case when $V_{SET} > 0$, hot electrons drift towards the silicon due to the gate electric field E applied by V_{SET} but are trapped in BN defects near the BN/SiO_2 interface. When there is enough charge in the BN trap states to screen the gate electric field, the charging process stops and the graphene becomes charge neutral at V_{SET} after e-beam exposure, as shown in Fig. 4c (top panel).

For high energy e-beam exposure (30 keV), electron-hole pairs are generated in both the bottom BN and SiO_2 ($d_p >> d_{BN}$, also see Supplementary Fig. S20), whereupon they separate due to the electric field E. With $V_{SET} > 0$, electron traps are activated in the BN near the BN/SiO_2 interface while hole traps are activated in the SiO_2 near the BN/SiO_2 interface. These charged traps reduce the potential drop but the total applied potential drop must equal V_{SET}, therefore more charge is accumulated in the dielectrics until an equilibrium distribution is reached. Since the SiO_2 layer is much thicker and has a higher defect density than the BN layer[19], more holes are trapped in SiO_2 than are electrons in BN as shown in Fig. 4c. Consequently, the combined doping effects of activated defects is opposite for a high (30 keV) vs. low (1 keV) energy e-beam. More control experiments and detailed discussion of the proposed mechanism are included in the SI (Supplementary Notes 11 - 14 and Figs. S19 - S23). This model can be also applied to MoS_2 to account for the similar energy-dependent reversed doping effects, but admittedly further development of the model is required to explain all subtleties of the doping behavior, for example asymmetries in p- and n-type doping behavior.

Conclusions

We have reported an e-beam doping technique for BN encapsulated van der Waals heterostructures. The technique provides a reversible method to write complex and non-volatile doping patterns with high spatial resolution, high carrier density, and high mobility, even at room temperature. We demonstrate this by directly writing p–n junctions and nanoscale patterns, as well as achieving electron and hole carrier densities beyond $\pm 10^{13}$ cm^{-2} with high mobility in a BN/graphene/BN heterostructure device. We also show similar controlled doping in MoS_2 devices. Our method provides a route to create multi-component nanoscale circuitry in vdW heterostructures with minimal processing. It may also be an ideal approach to pattern superlattice potentials or customize the electronic properties of 2D materials for novel scientific studies and device applications.

Methods

Device fabrication:

High quality BN crystals from Taniguchi and Watanabe are exfoliated onto 285 nm SiO_2/Si substrates. We use BN flakes ranging in thickness from 8 - 40 nm for the top and bottom encapsulating layers. The BN encapsulated graphene and MoS_2 van der Waals heterostructures are fabricated using the dry pick-up transfer technique[30] and then annealed in an Ar/H_2 forming gas for 3 hours at 350 ^{o}C. The top BN layer is mandatory for high mobility devices as it prevents environmental surface contamination from reaching the critical graphene layer (Supplementary Note 15 and Fig. S24). Standard

electron-beam lithography processes are used to pattern etching masks and electrodes onto the heterostructures. The thickness information for all the devices is provided in the SI (Supplementary Note 17, Table S1 and Fig. S25).

E-beam doping process:

The heterostructure device is mounted in a SEM (model: FEI XL30 Sirion) using a custom holder attached to an electrical feedthrough for doping and limited in-situ transport measurement (Supplementary Note 17 and Fig. S26). We use a standard ac voltage bias lock-in technique at 97.13 Hz to measure transport properties of the device in the SEM chamber under a vacuum of 3 x 10^{-6} mbar at room temperature. Electron beam energies range from 1 keV to 30 keV with beam current I_e ranging from 1 pA to 15 pA used for the e-beam induced doping.

Both normal scanning mode and lithography mode are implemented to study the doping effect and write pre-designed doping patterns on the BN encapsulated graphene and MoS_2 devices. For e-beam irradiation in the normal scanning mode, the exposed area S is about 300 μm^2 including the whole heterostructure region. Resistance is monitored during exposure and the exposure stopped when the irradiation induced resistance change has stabilized. Typical exposure time t ranges from 30 seconds to 120 seconds. The accumulated irradiation dosage D is given by $D = I_e t/Se$. For example, I = 10 pA, S = 300 μm^2, t = 60 seconds, then D = 200 $\mu C/cm^2$ (i.e., 12.5 e^-/nm^2). Once the resistance is stabilized under a certain preset voltage V_{SET} during irradiation, additional exposure will not cause further resistance changes. For lithography mode, we tested different dosage

parameters. To achieve high spatial resolution, a smaller dosage parameter is beneficial (Supplementary Notes 8 - 9 and Figs. S17 - S18).

Low-temperature transport measurements are performed in a Quantum Design PPMS after quickly transferring the doped sample from the SEM without significant exposure to ambient light (see Supplementary Note 5 and Fig. S12).

Near-field nano-imaging:

We employ a scattering-type scanning near-field optical microscope (s-SNOM) to obtain the near-field images of the samples. The s-SNOM is based on a tapping mode AFM. An infrared light beam (λ=10.6 μm) is focused onto the apex of a conductive AFM tip. An MCT detector placed in the far field is used to collect the scattered light, which carries local optical information of the sample. Near-field images are recorded simultaneously with the topographic information during the measurements. The optical contrast of doped and un-doped areas in the near-field images stem from their different local carrier densities, which result in different scattering amplitudes of the infrared light.

Data availability

The data that support the plots within this paper and other findings of this study are available from the corresponding author upon reasonable request.

References

1. Hu, C. *Modern semiconductor devices for integrated circuits*. (Pearson, 2010).
2. Novoselov, K. S. *et al.* Electric field effect in atomically thin carbon films. *Science*

306, 666–669 (2004).

3. Lui, C. H., Li, Z., Mak, K. F., Cappelluti, E. & Heinz, T. F. Observation of an electrically tunable band gap in trilayer graphene. *Nat. Phys.* **7**, 944–947 (2011).

4. Williams, J. R., DiCarlo, L. & Marcus, C. M. Quantum Hall effect in a graphene p-n junction. *Science* **317**, 638–641 (2007).

5. Özyilmaz, B. *et al.* Electronic transport and quantum hall effect in bipolar graphene p-n-p junctions. *Phys. Rev. Lett.* **99**, 2–5 (2007).

6. Huard, B. *et al.* Transport measurements across a tunable potential barrier in graphene. *Phys. Rev. Lett.* **98**, 8–11 (2007).

7. Liu, G., Velasco, J., Bao, W. & Lau, C. N. Fabrication of graphene p-n-p junctions with contactless top gates. *Appl. Phys. Lett.* **92**, 1–4 (2008).

8. Dubey, S. *et al.* Tunable superlattice in graphene to control the number of dirac points. *Nano Lett.* **13**, 3990–3995 (2013).

9. Efetov, D. K. & Kim, P. Controlling electron-phonon interactions in graphene at ultrahigh carrier densities. *Phys. Rev. Lett.* **105**, 2–5 (2010).

10. Ye, J. *et al.* Accessing the transport properties of graphene and its multilayers at high carrier density. *PNAS* **108**, 13002–13006 (2011).

11. Shi, W. *et al.* Superconductivity series in transition metal dichalcogenides by ionic gating. *Sci. Rep.* **5**, 1–10 (2015).

12. Zhao, S. Y. F. *et al.* Controlled electrochemical intercalation of graphene/ h-BN van der Waals heterostructures. *Nano Lett.* **18**, 460–466 (2018).

13. Xia, Y., Xie, W., Ruden, P. P. & Frisbie, C. D. Carrier localization on surfaces of organic semiconductors gated with electrolytes. *Phys. Rev. Lett.* **105**, 36802

(2010).

14. Ovchinnikov, D. *et al.* Disorder engineering and conductivity dome in ReS2 with electrolyte gating. *Nat. Commun.* **7**, 1–7 (2016).

15. Lohmann, T., Von Klitzing, K. & Smet, J. H. Four-terminal magneto-transport in graphene p-n junctions created by spatially selective doping. *Nano Lett.* **9**, 1973–1979 (2009).

16. Ojeda-Aristizabal, C. *et al.* Molecular arrangement and charge transfer in C60/graphene heterostructures. *ACS Nano* **11**, 4686–4693 (2017).

17. Ju, L. *et al.* Photoinduced doping in heterostructures of graphene and boron nitride. *Nat. Nanotechnol.* **9**, 348–352 (2014).

18. Velasco, J. *et al.* Nanoscale control of rewriteable doping patterns in pristine graphene/boron nitride heterostructures. *Nano Lett.* **16**, 1620–1625 (2016).

19. Wong, D. *et al.* Characterization and manipulation of individual defects in insulating hexagonal boron nitride using scanning tunnelling microscopy. *Nat. Nanotechnol.* **10**, 949–953 (2015).

20. Zhou, Y. *et al.* Programmable graphene doping via electron beam irradiation. *Nanoscale* **9**, 8657–8664 (2017).

21. Childres, I. *et al.* Effect of electron-beam irradiation on graphene field effect devices. *Appl. Phys. Lett.* **97**, 173109 (2010).

22. Yu, X., Shen, Y., Liu, T., Wu, T. & Jie Wang, Q. Photocurrent generation in lateral graphene p-n junction created by electron-beam irradiation. *Sci. Rep.* **5**, 1–8 (2015).

23. Iqbal, M. Z., Anwar, N., Siddique, S., Iqbal, M. W. & Hussain, T. Formation of

pn-junction with stable n-doping in graphene field effect transistors using e-beam irradiation. *Opt. Mater.* **69**, 254–258 (2017).

24. Stará, V., Procházka, P., Mareček, D., Šikola, T. & Čechal, J. Ambipolar remote graphene doping by low-energy electron beam irradiation. *Nanoscale* **10**, 17520–17524 (2018).

25. Teweldebrhan, D. & Balandin, A. A. Modification of graphene properties due to electron-beam irradiation. *Appl. Phys. Lett.* **94**, 92–95 (2009).

26. Hwang, E. H. & Sarma, S. Das. Acoustic phonon scattering limited carrier mobility in two-dimensional extrinsic graphene. *Phys. Rev. Lett.* **77**, 1–6 (2008).

27. Katagiri, Y. *et al.* Gate-tunable atomically thin lateral MoS_2 Schottky junction patterned by electron beam. *Nano Lett.* **16**, 3788–3794 (2016).

28. Xie, X. *et al.* Designing artificial 2D crystals with site and size controlled quantum dots. *Sci. Rep.* **7**, 1–7 (2017).

29. Sule, N. & Knezevic, I. Phonon-limited electron mobility in graphene calculated using tight-binding Bloch waves. *J. Appl. Phys.* **112**, 053702 (2012).

30. Wang, L. *et al.* One-dimensional electrical contact to a two-dimensional material. *Science* **342**, 614–617 (2013).

31. Ausman, G. A. & McLean, F. B. Electron-hole pair creation energy in SiO_2. *Appl. Phys. Lett.* **26**, 173–175 (1975).

32. Curtis, O. L., Srour, J. R. & Chiu, K. Y. Hole and electron transport in SiO_2 films. *J. Appl. Phys.* **45**, 4506–4513 (1974).

Acknowledgements:

This work was supported in part by the Director, Office of Science, Office of Basic Energy Sciences, Materials Sciences and Engineering Division, and Molecular Foundry of the U.S. Department of Energy under Contract No. DE-AC02-05-CH11231, primarily within the van der Waals Heterostructures Program (KCWF16) which provided for development of the concept and device fabrication, e-beam doping, and transport characterization, and within the sp2-Bonded Materials Program (KC2207) which provided for s-SNOM measurements; and by the National Science Foundation, under Grant No.1542741 which provided for AFM topography and SdH measurements, and under Grant No.1807233 which provided for EFM measurements.

Author contributions:

A.Z., M.C., W.S., S.K., H.-Z.T., D.W. conceived the experiment. S.K., W.S. and S.-Y. W. contributed to device fabrication. W.S. and S.K. performed all electrical measurements, EFM measurements, and data analysis. K.W. and T.T. provided the BN crystals. L.L.J. and F.W. contributed to the s-SNOM measurement. W.S., S.K. and A.Z. co-wrote the manuscript with inputs and comments from all authors.

Competing interests:

The authors declare no competing interests.

Figures

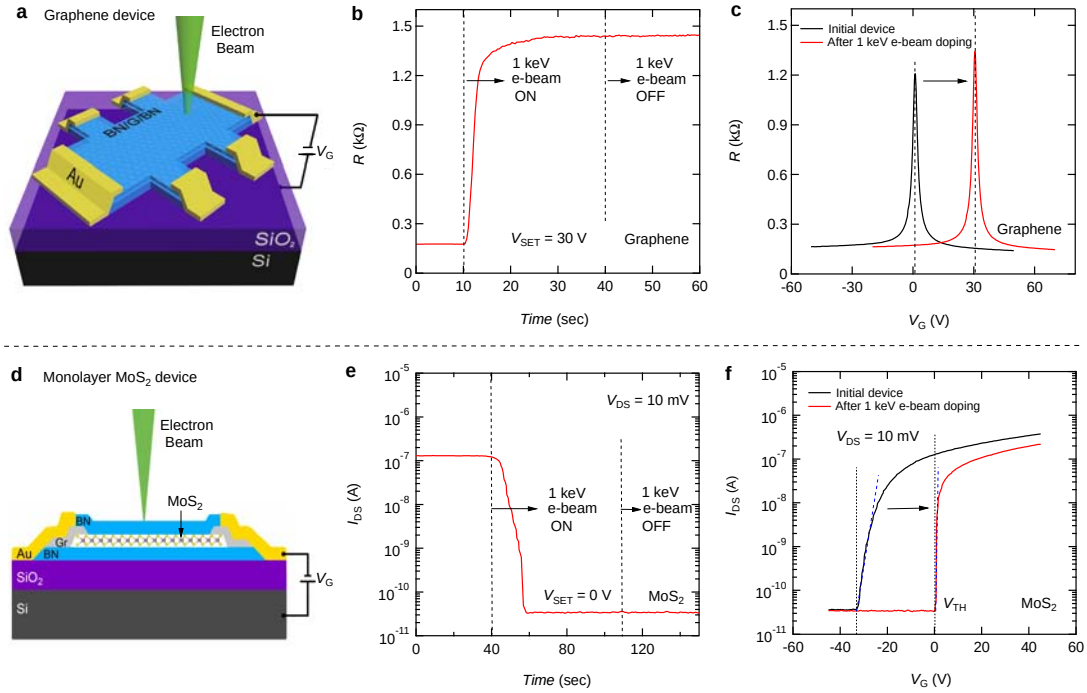

410

411 **Figure 1 | E-beam induced doping effect in graphene and MoS_2 van der Waals**

412 **heterostructures. a**, Experimental scheme for e-beam induced doping in graphene

413 device. Charge doping is induced in BN/Gr/BN by exposing it to a scanning electron

414 beam (1-30 keV) in a standard SEM for a few seconds while holding the back-gate

415 voltage $V_G \neq 0$ V. **b**, Resistance change of monolayer (ML) graphene (Device #1) when

416 a 1 keV e-beam is switched on and off (controlled by beam blanker in the SEM) with V_G

417 set to 30 V. V_{DS} = 50 μV for the graphene measurements. **c**, Transfer curves $R(V_G)$ of the

418 ML graphene before and after e-beam exposure. The CNP value is shifted from 0 V to 30

419 V (=V_{SET}), and the graphene has become uniformly hole doped. **d**, Cross-sectional view

420 of experimental scheme for e-beam doping in BN encapsulated ML MoS_2 transistor

421 device with multilayer graphene contacts. **e**, Source-drain current I_{DS} change of ML

422 MoS_2 when a 1 keV e-beam is switched on and off with V_G set to 0 V. **f**, $I_{DS}(V_G)$ of ML

423 MoS_2 before and after e-beam exposure. The threshold voltage V_{TH} is shifted from -33 V

to 0 V (=V_{SET}), and the calculated subthreshold swing (SS) decreases more than one order of magnitude after doping (see Fig. S4).

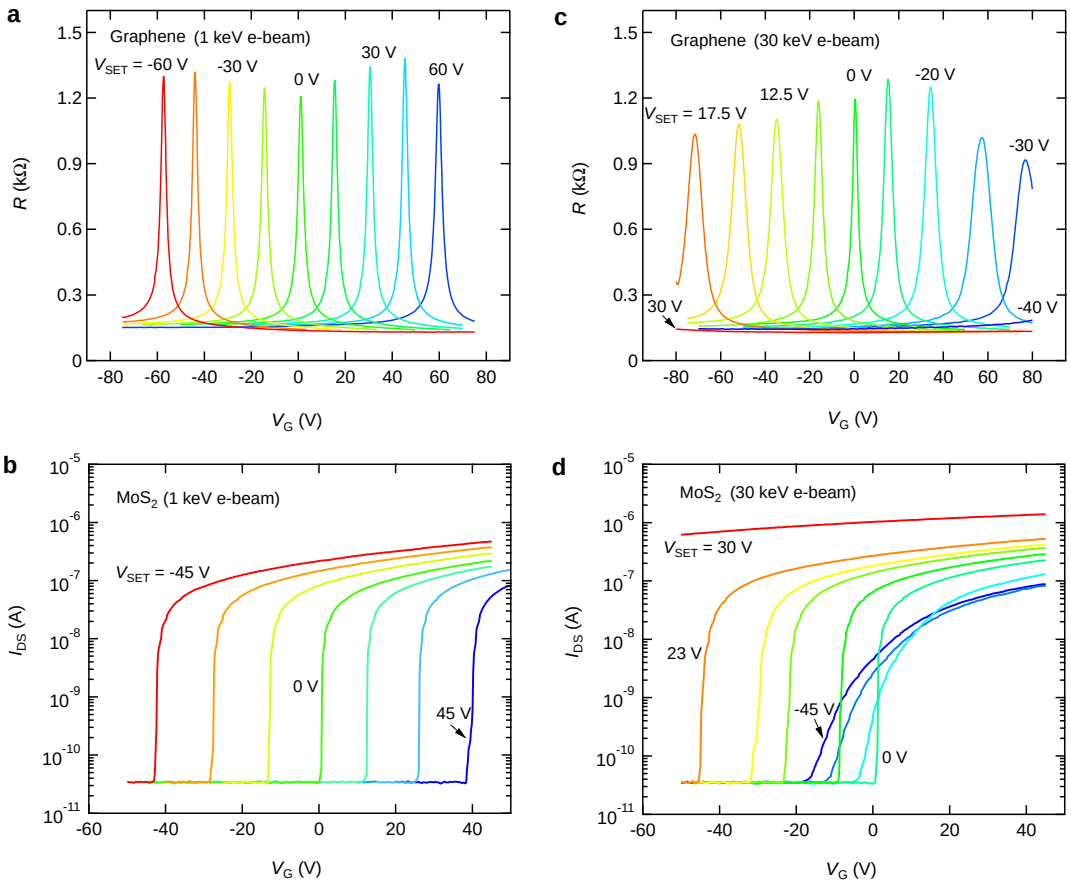

Figure 2 | Energy dependence of e-beam induced doping effect in graphene and MoS_2 van der Waals heterostructures. a, Transfer curves $R(V_G)$ of graphene following successive e-beam-induced doping using an e-beam energy of 1 keV. V_{SET} = -60, -45, -30, -15, 0, 15, 30, 45, 60 V, respectively (from red to blue). **b**, $I_{DS}(V_G)$ of ML MoS_2 after e-beam exposure using an e-beam energy of 1 keV. V_{SET} = -45, -30, -15, 0, 15, 30, 45, respectively (from red to blue). V_{DS} = 10 mV for the MoS_2 measurements. **c**, Same as in **a** but using a beam energy of 30 keV. V_{SET} = 30, 17.5, 15, 12.5, 10, 0, -10, -20, -25, -30, -

40 V, respectively (from red to blue). **d**, Same as in **b** but using a beam energy of 30 keV. V_{SET} = 30, 23, 22, 21, 20, 0, -15, -30, -45 V, respectively (from red to blue).

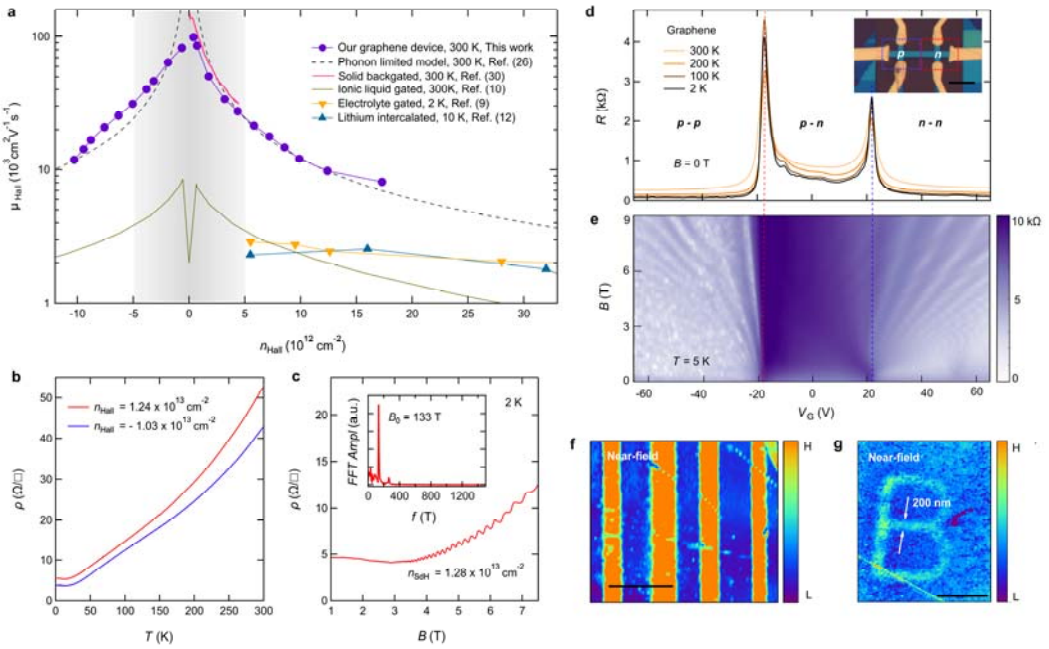

Figure 3 | Transport characteristics and spatially controlled nanoscale doping patterns of BN/Gr/BN heterostructures by e-beam induced doping. a, Hall effect mobility vs carrier density for 30 keV e-beam doped monolayer (ML) graphene samples at 300 K compared to other highly doped ML graphene samples reported in literature. Grey shaded region indicates conventional back-gate accessible carrier density regime. **b**, Four-terminal sheet resistivity ρ of 30 keV e-beam highly electron and hole-doped ML graphene devices, showing metallic behavior. **c**, ρ of electron-doped device in **b** measured as a function of magnetic field B at 2 K, showing well-defined periodic SdH oscillations. The corresponding carrier density n_{SdH} is 1.28 x 10^{13} cm^{-2}, derived from the peak position of the Fourier transform as shown in the inset. **d**, Generation of a p-n junction in BN/Gr/BN heterostructure by controlled e-beam exposure in lithography

mode. Temperature dependence of four-terminal resistance R versus V_G measured after writing the p-n junction at 300 K. Inset shows the device geometry. The scale bar is 5 μm. **e,** Log scale plot of longitudinal four-terminal resistance R of the graphene p-n junction as a function of magnetic field and gate voltage at 5 K. **f** and **g,** s-SNOM images of a stripe pattern and a letter "B" pattern written in a BN/Gr/BN heterostructure using 2 keV e-beam at V_{SET} = 55 V. The scale bar is 2 μm in **f** and 1 μm in **g**. The spatial resolution is about 200 nm indicated by the arrows in **g**.

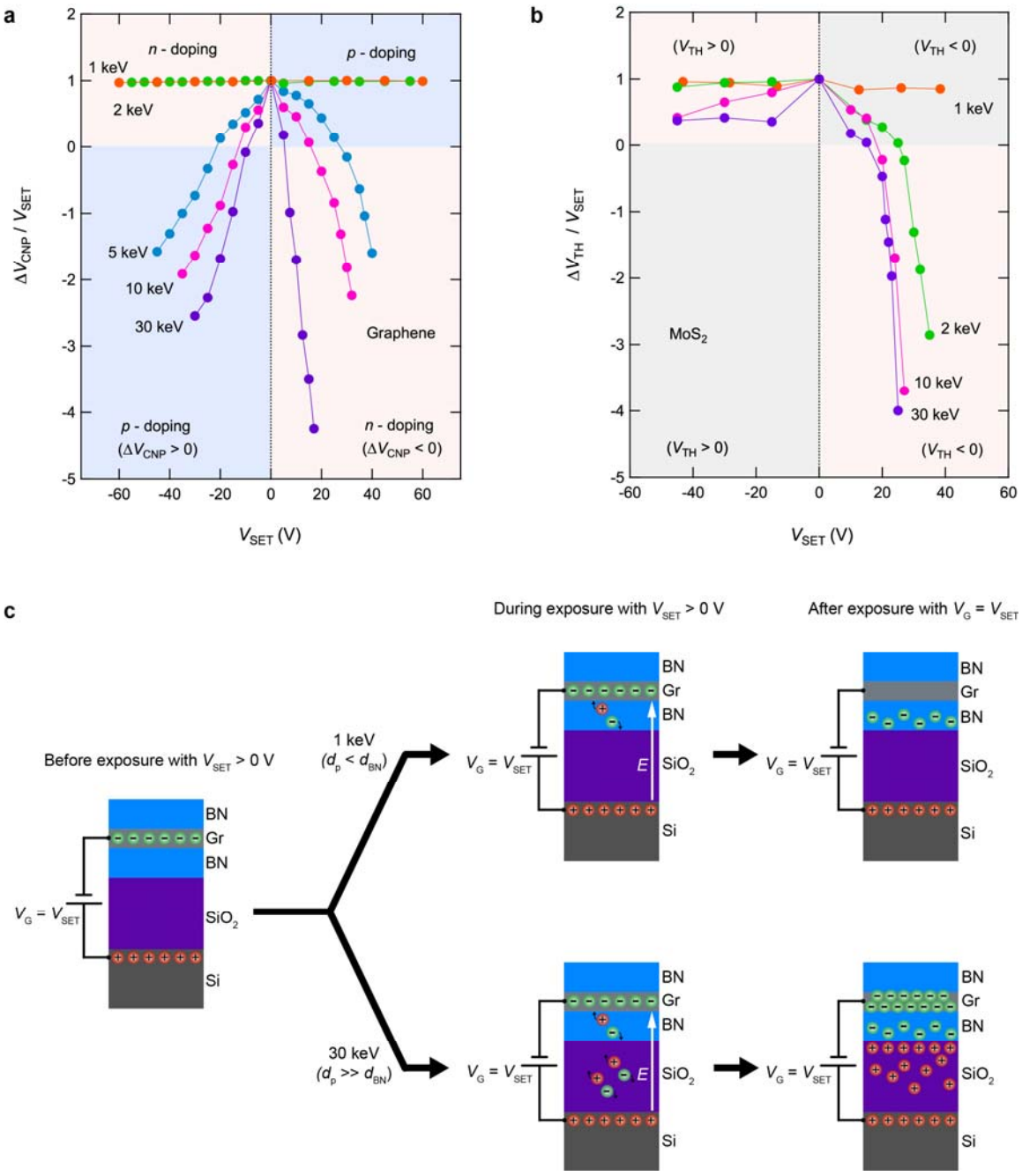

Figure 4 | Energy dependence and proposed mechanism for e-beam induced doping effect in graphene and MoS_2 vdW heterostructures. a, Normalized effective capacitance defined as $\Delta V_{CNP}/V_{SET}$ versus the corresponding V_{SET} for the e-beam doping effect in graphene at different e-beam energies. Red and blue shaded regions indicate electron and hole doping induced by e-beam exposure, respectively. **b**, Normalized

effective capacitance defined as $\Delta V_{TH}/V_{SET}$ versus V_{SET} for the e-beam doping effect in ML MoS_2 at different e-beam energies. **c**, Schematic of the doping process and charge carrier distribution for 1 keV and 30 keV e-beam doping in BN/Gr/BN at a positive V_{SET}. Here, d_p is the penetration depth of the electron beam and d_{BN} is the total BN thickness. In both scenarios, the device is kept at $V_G = V_{SET}$ after e-beam exposure. More detailed schematic of the doping process is included in the SI (Supplementary Figs. S22 and S23).